HHS Public Access

Author manuscript

Magn Reson Med. Author manuscript; available in PMC 2022 August 11.

Published in final edited form as:

Magn Reson Med. 2021 December ; 86(6): 3292–3303. doi:10.1002/mrm.28923.

Displacement current distribution on a high dielectric constant helmet and its effect on RF field at 10.5 T (447 MHz)

Navid P. Gandji[1], **Christopher T. Sica**[1], **Michael T. Lanagan**[2], **Myung-Kyun Woo**[3], **Lance DelaBarre**[3], **Jerahmie Radder**[3], **Bei Zhang**[4], **Riccardo Lattanzi**[5], **Gregor Adriany**[3], **Kamil Ugurbil**[3], **Qing X. Yang**[1]

[1]Center for NMR Research, Departments of Neurosurgery and Radiology, College of Medicine, Pennsylvania State University, Hershey, Pennsylvania, USA

[2]Department of Engineering Science and Mechanics, Pennsylvania State University, State College, Pennsylvania, USA

[3]Center for Magnetic Resonance Research, University of Minnesota, Minneapolis, Minnesota, USA

[4]UT Southwestern Medical Center, Advance Imaging Research Center, Dallas, Texas, USA

[5]Center for Advanced Imaging Innovation and Research (CAI2R) and Bernard and Irene Schwartz Center for Biomedical Imaging, Department of Radiology, New York University School of Medicine, New York, New York, USA

Abstract

Purpose: Investigating the designs and effects of high dielectric constant (HDC) materials in the shape of a conformal helmet on the enhancement of RF field and reduction of specific absorption rate at 10.5 T for human brain studies.

Methods: A continuous and a segmented four-piece HDC helmet fit to a human head inside an eight-channel fractionated-dipole array were constructed and studied with a phantom and a human head model using computer electromagnetic simulations. The simulated transmit efficiency and receive sensitivity were experimentally validated using a phantom with identical electric properties and helmet-coil configurations of the computer model. The temporal and spatial distributions of displacement currents on the HDC helmets were analyzed.

Results: Using the continuous HDC helmet, simulation results in the human head model demonstrated an average transmit efficiency enhancement of 66%. A propagating displacement current was induced on the continuous helmet, leading to an inhomogeneous RF field enhancement in the brain. Using the segmented four-piece helmet design to reduce this effect, an average 55% and 57% enhancement in the transmit efficiency and SNR was achieved in human head, respectively, along with 8% and 28% reductions in average and maximum local specific absorption rate

Correspondence: Qing X. Yang, Department of Neurosurgery, College of Medicine, Pennsylvania State University, 500 University Dr., NMR Research Facility, Hershey, PA 17033-2360, USA. qyang@psu.edu.

SUPPORTING INFORMATION

Additional Supporting Information may be found online in the Supporting Information section.

Conclusion: The HDC helmets enhanced the transmit efficiency and SNR of the dipole array coil in the human head at 10.5 T. The segmentation of the helmet to disrupt the continuity of circumscribing displacement currents in the helmet produced a more uniform distribution of the transmit field and lower specific absorption rate in the human head compared with the continuous helmet design.

Keywords

high dielectric constant material; SAR reduction; SNR enhancement; ultrahigh-field MRI

1 | INTRODUCTION

The development of ultrahigh magnetic field MRI system is primarily motivated by gaining a higher image SNR such that a greater spatial-temporal resolution for in vivo imaging of human body can be achieved.[1] With the advent of a 10.5T human system, new challenges in RF engineering were encountered, in which overall SAR is expected to increase significantly and the local SAR distribution can become more complicated to manage as a result of the stronger wave effects.[2–6] As anticipated from the previous experiences during the development of the 7T human system in the early years of 2000,[7–11] it is critically important to further develop novel RF technologies for the corresponding frequency regime for 10.5T human imaging. Although higher magnetic fields lead to substantial increases in ultimate intrinsic SNR,[12–15] capturing this ultimate intrinsic SNR is not easy and requires optimal RF coils. It is of great interest to explore the potential improvements in ultimate intrinsic SNR possible at a given field strength with HDC materials, considering the relative cost of further increasing field strength. Therefore, efforts to increase the magnetic fields need to be complimented with synergistic engineering efforts to improve the sensitivity and efficiency of signal detection. Here we report on the initial step toward the use of high dielectric constant (HDC) materials at 10.5 T, the highest magnetic field available currently for human experiments, to increase image SNR and enhance the RF field transmission efficiency.

HDC materials have previously been used to enhance performances of standard commercial RF coils for lower magnetic fields[16–20] and 7 T with various geometrical shapes (flexible pads and rigid blocks) with different HDC materials (pure water, slurries, and ceramics).[21,22] In recent efforts toward whole-cortex enhancement, HDC helmets have been developed and demonstrated an overall increase in B_1^+ field and SNR in the human brain at 3 T and 7 T.[23–25] The translation of this technology to 10.5 T is not straightforward because, at such a high magnetic field, the wavelength of the RF field used at the proton resonance frequency becomes much shorter in the human head (with an average dielectric constant of $\varepsilon_r = 47$ considering the brain white-matter and gray-matter dielectric constant values at 447 MHz are 41.5 and 56.6, respectively) and even shorter in HDC materials. Under such a condition, it is uncertain how the induced displacement currents in a HDC conformal helmet would form in response to the RF fields generated by the transmission coils, and how HDC materials, acting as a secondary field source, would impact the resultant electric and magnetic field distributions in the human head, and related safety issues.

To begin addressing these new engineering questions introduced by the combined use of 10.5 T and HDC materials, in this work we investigated displacement current distributions in two HDC conformal helmets positioned inside a dipole antenna array, and their effects on the RF field behaviors in the human head using numerical electromagnetic (EM) simulations and phantom experiments. The simulated transmit efficiency and receive sensitivity at 447 MHz with and without the HDC helmets were experimentally evaluated using a phantom approximating a human head at 10.5 T. Subsequently, the transmit efficiency, receive sensitivity, and specific absorption rate (SAR) in a virtual human head model under the same coil-helmet configurations were evaluated with EM simulations. The results demonstrate that significant gains can be obtained with incorporation of HDC materials into RF coils at 10.5 T.

2 | METHODS

2.1 | Experimental design

2.1.1 | Radiofrequency coil—An eight-channel dipole antenna array attached to a cylindrical polyethylene terephthalate glycol-modified former with a diameter of 277 mm was used (Figure 1A). Each transmit element consisted of a dipole antenna printed on an FR4 circuit board (Figure 1B). Each element of the eight-channel dipole antenna array was tuned to 447 MHz. The length of dipole antenna was 18 cm (Figure 1B) with a fractionated structure to reduce local SAR and the physical length of the dipole antenna.[26] Two inductors at the feed point were used for fine-tuning of individual elements of the eight-channel dipole antenna array. A lattice balun matching network consisting of two 10-pF series capacitors (100B series; American Technical Ceramics, Huntington Station, NY) and two 12.8-nH inductors were used in all elements.

2.1.2 | Phantom—A lightbulb-shaped phantom approximating an average human head geometry and electric property was constructed for both EM modeling and performing experimental validations. This phantom study is a mandatory step for the safety assurance of performing in vivo human head experiments at 10.5 T (at the time these experiments were performed). The phantom had a circular cross section with a maximum diameter of 176 mm at the center and a height of 234 mm. The phantom material consisted of a homogenous PVP agar gel mixture. Measured values of the permittivity and the conductivity of the phantom were $\varepsilon_r = 47.3$ and $\sigma = 0.65$ S/m, obtained using a DAKS-12 coaxial dielectric probe (SPEAG AG, Zurich, Switzerland) at 447 MHz. These values mimic the average electrical properties of the human brain at this frequency. The T_1 relaxation time of the phantom at 10.5 T was measured at 260 ms.

2.1.3 | High-dielectric constant helmet—A helmet shaped shell (Figure 1C) was printed and filled with HDC material. The shell consisted of an oval-shaped cylinder with a dome on top. The height of the cylinder was 100 mm, and the height of the dome was 100 mm (overall height was 200 mm). The HDC material for the purpose of simulation and experiment was distilled water ($\varepsilon_r = 78$ and $\sigma = 5^{-6}$ S/m). The thickness of the distilled water as the HDC material is 8 mm, contained in a polylactic acid 3D-printed former with a 2-mm thick wall. Two different HDC helmet designs were investigated: a continuous HDC

helmet (helmet 1) and a segmented four-piece HDC helmet (helmet 2), as illustrated in Figure 1C,D, respectively. Because the presence of HDC helmets has an effect on the tuning and matching of the RF coil, each coil antenna element was tuned and matched individually without and with the presence of either helmet 1 or helmet 2.

2.2 | B_1^+ and SNR map acquisition

All experiments were carried out on a Siemens 10.5T scanner (Siemens Healthineers, Erlangen, Germany). The eight-channel fractionated dipole array was used for both transmission and reception. Transmission used a circular polarization (CP), achieved by setting a sequential 45° phase difference between transmit channels. The power delivered to each transmit channel was measured by the Siemens power monitor integrated into the system.

The B_1^+ transmit efficiency maps were collected with an implementation of the actual flip-angle imaging method,[27] based on a 3D spoiled gradient-echo sequence with the following parameters: TR1/2 = 22/122 ms, TE = 2.03 ms, flip angle = 60°, voxel size = 1.5 × 3 × 3 mm, and FOV = 354 × 354 × 264 mm. Additionally, a geometrically matched 2D spoiled gradient-echo sequence was acquired for calculation of SNR maps, with the following parameters: TR = 4000 ms, TE = 3.00 ms, flip angle = 50°-70°, voxel size = 1.5 × 3 mm, FOV = 354 × 354 mm, slice thickness = 3 mm, and number of slices = 88. A separate noise scan with bandwidth matched parameters was acquired for calculation of the noise covariance matrix. The SNR Units method[28] was subsequently applied to calculate the SNR maps. These maps were divided by the sine of the acquired flip-angle map to remove the influence of the flip angle on the SNR value. Data processing in this step used custom-built programs in *IDL* 8.7.1 (Harris Corporation, Melbourne, FL).

2.3 | Electromagnetic simulations

All simulations were performed using *Microwave Studio* (Computer Simulation Technology, CST, Darmstadt, Germany), a numerical full wave EM field solver based on the finite integration technique method. The simulations were performed first with a phantom with specific electric properties that matched those of an average human head (see previously) for experimental validations at 10.5 T. Subsequently, simulations in a human head model (Ella)[29] were performed to predict the RF coil performance and enhancement in the human head with different HDC helmet designs. Each of the eight elements was simulated separately, followed by combination of the fields from each element to obtain the total field.

The transmit efficiency was calculated by dividing the total B_1^+ field in CP mode over the total accepted power by the RF coil antenna array[30] as follows:

$$B_{1efficiency}^{+} = \frac{\sum_{n=1}^{8} B_{1n}^{+} e^{-j(n-1)\pi/4}}{\sqrt{\sum_{n=1}^{8} P_{accn}}} \quad (1)$$

where n is the channel number, and $P_{acc\,n}$ is the accepted power by each channel of the coil array. SNR was calculated with a noise covariance-weighted root sum of squares

reconstruction, using the simulated B_1^- and noise covariance matrix.[28,31] The SAR was defined as the rate of energy dissipation due to induced electric field, E, in the sample[32] as follows:

$$SAR = \frac{\sigma_i \left| \sum_{n=1}^{8} \overrightarrow{E_{in}} \right|^2}{2\rho_i} \quad (2)$$

where σ_i and ρ_i are the conductivity and mass density, and E_{in} is the electric field from each channel at voxel i. Local SAR was calculated on a per-voxel basis, and 10g SAR is defined as the averaged SAR over a 10-g mass of the tissue.[33]

3 | RESULTS

3.1 | Phantom simulation and experiment

Figure 2 shows the comparison of the simulated and experimental results for B_1^+ efficiency ($\mu T/\sqrt{W}$, where W is the accepted power) and SNR in the phantom in three orthogonal planes. The B_1^+ efficiency map was acquired when the coil array was driven in CP mode with 45° phase difference between adjacent coil elements.

As shown in Figure 2, with CP mode excitation, the B_1^+ efficiency distribution exhibited a characteristic pattern in this phantom: a bright center surrounded by a dark ring in the axial image due to the constructive and destructive interferences of the propagating attenuated RF waves emanating from each of the eight dipole elements.[34] With HDC helmet 1, the overall B_1^+ efficiency was significantly enhanced with an intense signal in the central regions where the transmission RF field by each element was coherently superimposed. The most prominent enhancement is seen on the top of the phantom (top, as defined in the coronal and sagittal images, corresponding to the top of the head in the case of human head imaging). The higher B_1^+ field induced by the HDC helmet 1 at the top and, to a lesser extent, in the peripheral regions of the phantom seen in the coronal and sagittal planes, leads to a "U-shaped" low B_1^+ region surrounding the central high B_1^+ spot in these slice orientations. Apart from some identifiable artifacts, the computer modeling reproduced these features in the experimental B_1^+ distributions remarkably well for both cases,

Also shown in Figure 2, the SNR or receive sensitivity was significantly improved by the HDC helmet 1, particularly in the superior portion of the phantom, leading to a more uniform distribution. Accordingly, the quantitative comparisons between the experimental results obtained with helmet 1 and the baseline in the transmit efficiency and SNR in the same region of interest in the phantom are given in Table 1. The overall SNR enhancements by the HDC helmet 1 in this phantom was approximately 45% in the region of interest. The experimentally measured SNR maps also show a similar pattern of enhancement apart from some discernable artifacts (dark ring in the axial and dark bands in the coronal and sagittal images). These artifacts were caused because SNR was calculated to be independent

of B_1^+ magnitude (ie, normalized to B_1^+) and regions where the B_1^+ was too weak (typically caused by the strong signal modulation due to transmission field inhomogeneity as seen in the previous B_1^+ maps) were excluded from the SNR calculations.

Figure 3 displays the corresponding SAR maps, calculated from simulated results. Overall SAR was visibly reduced by the HDC helmet 1, and the SAR distribution was also changed considerably. It is notable that a relatively higher SAR region seen as a concentric ring in the axial plane in the baseline case was transformed into a high plateau near the top of the phantom with the HDC helmet 1.

3.2 | Displacement current simulations

As described previously, the enhancement by the HDC material was a result of induced displacement current within the material.[20] The region with intense SAR in the presence of the helmet in Figure 3 corresponds to the stronger B_1^+ on top of the phantom in Figure 2, both of which are caused by the induced displacement current in helmet 1. To understand the characteristics of B_1^+ enhancement by the continuous structure of HDC material, Figure 4A shows the displacement current distribution in helmet 1 at four phases in a cycle under the CP mode of the transmit dipole array.

A displacement current swirl was formed over the helmet, which rotates and propagates in time following the coil's CP field. The "center of the swirl (blue spot)" corresponds to where the B_1^+ is the strongest. As a result of the continuity of current flow, a persistently strong displacement current was formed on the top portion of the helmet for all phases of CP field, which leads to the prominent B_1 as well as SNR enhancement on top of the phantom. Conversely, this focal enhancement in RF field also leads to a local SAR increase, as shown in Figure 3.

To reduce the undesirable elevation of local SAR, helmet 1 was divided into four equal segments to disrupt the current flow and restrict it within each segment. In this segmented helmet design, denoted as helmet 2, the impedance change in the gaps between the segments effectively confined the propagation of displacement current within each segment (Figure 4B), so that the large displacement current on the top of helmet 1 was eliminated.

In Figure 4A, however, the traveling wave behavior of displacement current is intermingled with the rotational field of CP transmission field. To show the propagating wave more explicitly, the instantaneous distribution of the displacement current intensity amplitude, $|J|$, in helmet 1 and 2, induced by only one of the elements of the dipole array, are shown in Figure 4C,D, respectively. In addition, the z component of the displacement current in the helmets, J_{dz}, which produces the transverse B_1 predominantly in the sample, is also shown in Figure 4E,F. In this case, J_{dz} can be seen propagating around the helmet from the coil element. Clearly, the secondary RF field formed by the induced displacement current is no longer local and with a phase delay or retardation over helmet 1. This effect is significantly attenuated by the discontinuity across the gaps in the segmented helmet 2. For a better visualization of the wave behavior, Supporting Information Figure S1 presents

videos of the corresponding temporal variations of displacement currents in helmet 1 and helmet 2, induced by the CP field of the coil array as well as by one of its elements. The displacement current distributions induced on the helmets were all obtained with a numerically tuned-and-matched condition of the coil array with loading of either the human head or the phantom. The displacement current distribution in the helmets in Figure 4 was obtained with the loaded human head model.

3.3 | Human head model simulations

Having validated phantom simulation results with experiments, numerical modeling was performed on a human head model[29] with the identical setup. Figure 5 illustrates the calculated B_1^+ efficiency and SNR maps in the human head for baseline, with HDC helmet 1 and Helmet 2.

Compared with the phantom results in Figure 2, the B_1^+ efficiency and SNR distributions in the human head were represented remarkably well by those obtained with the phantom, particularly in the coronal plane. Because the human head generally does not possess cylindrical symmetry as the phantom, the ring of low B_1^+ seen in the axial plane in the phantom with helmet 1 (Figure 2) manifested as a parenthesis-shaped pattern in the head (Figure 5, middle row). Like the phantom case, a U-shaped lower-intensity B_1^+ pattern surrounding a central high-field region was evident in the coronal plane in the human head simulations with both helmets. Similar to the phantom results, HDC helmet 1 produced a strong B_1^+ enhancement on top of the head (Figure 4, middle row). This enhancement was significantly reduced in the case of HDC helmet 2, and the resulting B_1^+ efficiency map was more uniform, as predicted by the displacement current simulations (Figure 4).

Figure 6 shows the SAR maps corresponding to the three cases. The focal enhancement of B_1^+ efficiency by HDC helmet 1 on the top of the head led to a local SAR increase near this region, as observed in the phantom; both average and maximum SAR were significantly reduced from 0.26 W/kg and 0.78 W/kg for the baseline to 0.24 W/kg and 0.56 W/kg by the segmented HDC helmet 2.

The quantitative comparisons of 10g-SAR and B_1^+ efficiency within the brain for the baseline, HDC helmet 1 and helmet 2 in the region of interest are provided in Table 2.

4 | DISCUSSION

This work is an initial attempt in incorporating a HDC helmet to improve RF coil performance for human brain imaging at 10.5 T. The work is motivated by the desire to achieve a greater image resolution, as current MRI resolutions fall far short of the spatiotemporal scale over which brain circuits are organized and operate (eg, Insel et al[35]). To date, this challenge has been addressed primarily by increasing the magnetic field strength to exploit the field dependent increases in the SNR expected with higher magnetic fields. Such efforts have ultimately led to the development of 7 T[36] as a commercially

available instrument used both as a clinical scanner and an advanced platform for human research. Despite significant gains and consequent accomplishments, however, SNR remains relatively low even at 7 T compared with the challenges posed by the complexity of the brain's functional architecture. For example, at 7 T, imaging of neuronal activity in the brain (ie, functional MRI) reached the scale of submillimeter resolution functional mapping of cortical columns and layers, and other fine-scale organizations (Refs [36–38]). However, resolutions attained are marginally adequate for studying such mesoscopic organizations, and the SNR available at these resolutions remains suboptimal. This has led to efforts to pursue even higher fields,[39] despite the difficulties and rapidly increasing cost of building such ultrahigh-field (UHF; defined as ≥ 7 T) magnets capable of accommodating humans, culminating in the recent deployment of 10.5 T[40–42] for whole-body human imaging, and ongoing efforts to reach 11.7 T[39,43] and even higher magnetic fields.[39,44] A crucial experience learned from the development of 7 T, the efforts to gain SNR by increasing the static magnetic field need to be supported by synergistic RF engineering to improve the sensitivity and efficiency of signal detection while maintaining the safety of the human subjects at corresponding operating frequency.

For this endeavor, one foremost issue for using this system is the safety of the human subjects under the RF frequency regime. At present, 10.5 T is operated under a Food and Drug Administration Investigational Device Exemption, which requires the approval of each RF coil by the Food and Drug Administration; this process involves the submission of extensive EM simulations and experimental data on phantoms, and simulations with human head models, similar to what is presented in this paper. As such, one limitation of this study was the inability to perform human studies with the RF coil and HDC helmet setups reported here. Therefore, the experimental validation of simulation results could only be conducted with a phantom with appropriate electrical properties mimicking the human head. In this case, the experimental coil-sample configuration was modeled precisely, such that the results can be compared quantitatively with experimental data on the same construct.

As shown in Figure 2, the specific patterns of the B_1^+ maps in the three orthogonal planes were well reproduced between the simulations and the experimental data on the phantom. Because of the strong wave behavior of the RF field at 10.5 T, the interference patterns of the B_1^+ field in the sample by the CP configuration of the volume coil is uniquely determined by the geometry and electric properties of the sample. This offers quantitative metrics for comparing simulated field pattern with experiments. For example, the diameter of the dark ring seen in the axial plane is approximately equal to the RF field wavelength in the phantom ($\lambda_{phantom}$ = 97 mm), which was reproduced well in the experimental map. Thus, the experimental validation of B_1^+ (Figure 2 and Table 1) in the phantom provides a high confidence level for subsequent studies of the human brain with computer modeling. These EM calculations reveal that in the human brain, HDC materials in the form of helmet 1 and helmet 2 lead to 66% and 55% higher average B_1^+ efficiency, compared with baseline, respectively (Table 2), which provided a significant multiplier compared with other available engineering approaches for improving RF coil performance. Compared with the baseline, SNR increased by 20% and 57% for helmet 1 and helmet 2, respectively, although the

SNR gains are spatially less uniform in the latter case. Taking into account also the SAR performance (Table 2), helmet 2 clearly emerges as the preferred design with the dipole array coil.

The CP RF field created by the transmit coil induces a displacement current swirl distribution when the HDC material presents a continuous surface that can support such currents, as is the case with helmet 1 (Figure 4 and Supporting Information Figure S1). The circumference of HDC helmet 1 is about 641 mm at the middle of the helmet, which is more than 9-fold larger compared with the wavelength of a plane wave in a uniform medium of the same permittivity as the helmet (75.94 mm). The strong displacement current in the HDC material propagates as a wave over the continuous structure of the helmet while following the azimuthally rotating source field of the coil array. Thus, the induced displacement current is no longer locally distributed near the coil element that induces it. The displacement currents distributed over the helmet also have different phases that depend on the distance from the source coil element. The resultant RF field in the sample produced by this highly distributed displacement current in the helmet and the coil array appeared to spread out in time and become smoother in space. In a recent study, improved transmit efficiency using a helmet of HDC ceramic has been demonstrated at 7 T with computer modeling and in vivo human experiment. Interestingly, this study demonstrated improvements not only in transmit efficiency using an eight-channel dipole transmit array but also in SNR with a 28-channel receive array throughout the head, including at the center of the brain.[23,25] The observed SNR improvement in the center of the brain, where it is difficult to improve SNR by other means, could likely relate to such a propagating wave behavior over an HDC helmet structure. Thus, for optimization of the design of HDC material for high-field applications, it is necessary to further investigate propagating wave behavior of displacement current in a large continuous structure, such as the helmets presented here, and its influences on the RF field distribution in the human body.

Because the displacement current must obey the continuity principle, as does the conductive current, the induced displacement current must have a “return path” to form a completely closed loop. As a result of topology of the helmet, a persistently strong displacement current was formed on the top of HDC helmet 1, which led to the prominent B_1^+ and SNR enhancements on top of the phantom (Figure 2) and the human head (Figure 5). This focal enhancement in RF field also led to a corresponding increase in local SAR, as shown in Figure 6.

To minimize the detrimental elevation of local SAR by the concentrated displacement current distribution, the helmet was divided into four equal segments, such that the propagation of displacement current loop was disrupted and consequently confined within each segment of the HDC helmet 2.

As a result, the maximum SAR in the brain was reduced by 28%, whereas the transmit efficiency relative to baseline was enhanced by 55%, which is only marginally less than the 66% enhancement (relative to baseline) attained by HDC helmet 1 (Table 2). These data also illustrate the effect of the HDC material’s geometry following the performance of a RF coil incorporating such materials at 10.5 T. As shown previously, HDC materials can

be an effective passive shimming device for shaping the RF field distribution.[45] However, the physical mechanism of the current case is complicated by the propagation of the displacement current over the helmet structure. It is, therefore, necessary to optimize a RF coil design with consideration of the permittivity as well as the geometry of the HDC materials, along with coil designs for a given field strength.

The increase in the static magnetic field strength sought for SNR gains are normally accompanied by elevated losses in tissues at the correspondingly high RF frequency that must be used in the MR experiment. Thus, management of SAR is a critical challenge for realizing the potential of UHF MRI for human imaging applications. Parallel transmission has emerged as a solution for minimizing SAR while simultaneously improving B_1^+ inhomogeneity (eg, Refs [46–48]) needed for spatial uniformity of SNR and image contrast at UHF. Our results with HDC materials presented here indicate that incorporating such materials into RF coil design provides an alternative and complementary solution for reducing SAR, while increasing SNR at the same time. Such a path, however, must take into account the geometry of the HDC material incorporated into the RF coil, as demonstrated here. In this case, HDC helmet 2 is the preferred design in terms of B_1^+ efficiency, B_1^+ homogeneity, and SAR.

A caveat in the conclusions reached in this study is that the two RF coil-helmet configurations presented here are by no means optimized. This study is the first attempt in incorporating a HDC helmet with a simple dipole array at 10.5 T. The computer modeling revealed a new issue of propagating wave behavior of displacement current, and hinted a simple solution based on experiences and intuition. We expect that a greater improvement in both transmission efficiency and receive sensitivity could be achieved in the future with a systematic optimization. In addition, the eight-channel dipole array used for this study is not the optimal receiver with respect to receive sensitivity. Higher channel loop coil arrays have been shown to produce excellent SNR gains and image quality at UHF.[49,50] Evaluations of incorporating HDC materials into such dense receive arrays with a separate transmitter are currently under way and will be reported in the future.

5 | CONCLUSIONS

We explored the use of HDC materials in a conformal helmet configuration with a dipole array coil using computer modeling and experiment at 10.5 T. The simulated B_1^+ efficiency and receive sensitivity were experimentally validated carefully using a phantom with precisely measured and confirmed geometry and electric properties. The simulation on a human head model demonstrated that enhancements in both B_1 efficiency and SNR, and a significant reduction of SAR, could be achieved simultaneously by incorporating an HDC helmet into a transmit-receive dipole array at 10.5 T. Computer modeling revealed that a propagating displacement current wave formed on the HDC helmet when it was a continuous structure. As a secondary current source of RF field, the amplitude and phase distribution of the displacement current wave on the helmet could alter the RF field far from the primary current source. Such wave characteristics in the HDC material could not

only influence the optimal design of the coil-HDC helmet, but may also lead to a broader application for shaping or shimming the RF field for UHF human imaging.

Supplementary Material

Refer to Web version on PubMed Central for supplementary material.

Funding information

National Institutes of Health; Grant/Award No. U01 EB025144

REFERENCES

1. Ertürk MA, Wu X, Eryaman Y, et al. Toward imaging the body at 10.5 tesla. Magn Reson Med. 2017;77:434–443. [PubMed: 27770469]
2. Ibrahim TS, Abduljalil AM, Baertlein BA, Lee R, Robitaille PML. Analysis of B1 field profiles and SAR values for multi-strut transverse electromagnetic RF coils in high field MRI applications. Phys Med Biol. 2001;46:2545–2555. [PubMed: 11686274]
3. van Osch MJP, Webb AG. Safety of ultra-high field MRI: what are the specific risks? Curr Radiol Rep. 2014;2:61.
4. Sadeghi-Tarakameh A, Adriany G, Metzger GJ, et al. Improving radiofrequency power and specific absorption rate management with bumped transmit elements in ultra-high field MRI. Magn Reson Med. 2020;84:3485–3493. [PubMed: 32767392]
5. Wolf S, Diehl D, Gebhardt M, Mallow J, Speck O. SAR simulations for high-field MRI: how much detail, effort, and accuracy is needed? Magn Reson Med. 2013;69:1157–1168. [PubMed: 22611018]
6. Yang QX, Wang J, Zhang X, et al. Analysis of wave behavior in lossy dielectric samples at high field. Magn Reson Med. 2002;47:982–989. [PubMed: 11979578]
7. Vaughan JT, Garwood M, Collins CM, et al. 7T vs. 4T: RF power, homogeneity, and signal-to-noise comparison in head images. Magn Reson Med. 2001;46:24–30. [PubMed: 11443707]
8. Adriany G, Van de Moortele P-F, Wiesinger F, et al. Transmit and receive transmission line arrays for 7 Tesla parallel imaging. Magn Reson Med. 2005;53:434–445. [PubMed: 15678527]
9. Vaughan JT, Snyder CJ, DelaBarre LJ, et al. Whole-body imaging at 7T: preliminary results. Magn Reson Med. 2009;61:244–248. [PubMed: 19097214]
10. Wang J, Yang QX, Zhang X, et al. Polarization of the RF field in a human head at high field: a study with a quadrature surface coil at 7.0 T. Magn Reson Med. 2002;48:362–369. [PubMed: 12210945]
11. Yacoub E, Shmuel A, Pfeuffer J, et al. Imaging brain function in humans at 7 Tesla. Magn Reson Med. 2001;45:588–594. [PubMed: 11283986]
12. Guerin B, Villena JF, Polimeridis AG, et al. The ultimate signal-to-noise ratio in realistic body models. Magn Reson Med. 2017;78:1969–1980. [PubMed: 27917528]
13. Ocali O, Atalar E. Ultimate intrinsic signal-to-noise ratio in MRI. Magn Reson Med. 1998;39:462–473. [PubMed: 9498603]
14. Wiesinger F, Boesiger P, Pruessmann KP. Electrodynamics and ultimate SNR in parallel MR imaging. Magn Reson Med. 2004;52:376–390. [PubMed: 15282821]
15. Schnell W, Renz W, Vester M, Ermert H. Ultimate signal-to-noise ratio of surface and body antennas for magnetic resonance imaging. IEEE Trans Antennas Propag. 2000;48:418–428.
16. Yang QX, Wang J, Wang J, Collins CM, Wang C, Smith MB. Reducing SAR and enhancing cerebral signal-to-noise ratio with high permittivity padding at 3 T. Magn Reson Med. 2011;65:358–362. [PubMed: 21264928]
17. Brink WM, Webb AG. High permittivity pads reduce specific absorption rate, improve B1 homogeneity, and increase contrast-to-noise ratio for functional cardiac MRI at 3 T. Magn Reson Med. 2014;71:1632–1640. [PubMed: 23661547]

18. Brink WM, van den Brink JS, Webb AG. The effect of high-permittivity pads on specific absorption rate in radiofrequency-shimmed dual-transmit cardiovascular magnetic resonance at 3T. J Cardiovasc Magn Reson. 2015;17:82. [PubMed: 26385206]
19. Rupprecht S, Sica CT, Chen W, Lanagan MT, Yang QX. Improvements of transmit efficiency and receive sensitivity with ultrahigh dielectric constant (uHDC) ceramics at 1.5 T and 3 T. Magn Reson Med. 2018;79:2842–2851. [PubMed: 28948637]
20. Sica CT, Rupprecht S, Hou RJ, et al. Toward whole-cortex enhancement with a ultrahigh dielectric constant helmet at 3T. Magn Reson Med. 2020;83:1123–1134. [PubMed: 31502708]
21. Yang QX, Mao W, Wang J, et al. Manipulation of image intensity distribution at 7.0 T: passive RF shimming and focusing with dielectric materials. J Magn Reson Imaging. 2006;24:197–202. [PubMed: 16755543]
22. Haines K, Smith NB, Webb AG. New high dielectric constant materials for tailoring the B1+ distribution at high magnetic fields. J Magn Reson. 2010;203:323–327. [PubMed: 20122862]
23. Lakshmanan K, Walczyk J, Rupprecht S, et al. Improved brain imaging with an integrated high-permittivity material head array. In: Proceedings of the Annual Meeting of ISMRM [Virtual], 2020. Abstract #4083.
24. Teeuwisse WM, Brink WM, Haines KN, Webb AG. Simulations of high permittivity materials for 7 T neuroimaging and evaluation of a new barium titanate-based dielectric. Magn Reson Med. 2012;67:912–918. [PubMed: 22287360]
25. Lakshmanan K, Carluccio G, Walczyk J, et al. Improved whole brain SNR with an integrated high-permittivity material in a head array at 7T. Magn Reson Med. 2021;86:1167–1174. [PubMed: 33755236]
26. Raaijmakers AJE, Italiaander M, Voogt IJ, et al. The fractionated dipole antenna: a new antenna for body imaging at 7 Tesla. Magn Reson Med. 2016;75:1366–1374. [PubMed: 25939890]
27. Yarnykh VL. Actual flip-angle imaging in the pulsed steady state: a method for rapid three-dimensional mapping of the transmitted radiofrequency field. Magn Reson Med. 2007;57:192–200. [PubMed: 17191242]
28. Kellman P, McVeigh ER. Image reconstruction in SNR units: a general method for SNR measurement†. Magn Reson Med. 2005;54:1439–1447. [PubMed: 16261576]
29. Christ A, Kainz W, Hahn EG, et al. The virtual family—development of surface-based anatomical models of two adults and two children for dosimetric simulations. Phys Med Biol. 2010;55:N23–N38. [PubMed: 20019402]
30. Ertürk MA, Raaijmakers AJE, Adriany G, Uğurbil K, Metzger GJ. A 16-channel combined loop-dipole transceiver array for 7 Tesla body MRI. Magn Reson Med. 2017;77:884–894. [PubMed: 26887533]
31. Roemer PB, Edelstein WA, Hayes CE, Souza SP, Mueller OM. The NMR phased array. Magn Reson Med. 1990;16:192–225. [PubMed: 2266841]
32. Caputa K, Okoniewski M, Stuchly MA. An algorithm for computations of the power deposition in human tissue. IEEE Antennas Propag Mag. 1999;41:102–107.
33. IEC/IEEE International Standard. Determining the peak spatial average specific absorption rate (SAR) in the human body from wireless communications devices, 30 MHz to 6 GHz. Part 1: General requirements for using the finite-difference time-domain (FDTD) method for SAR calculations. IEC/IEEE 62704-1:2017;2017:1–86.
34. Van de Moortele PF, Akgun C, Adriany G, et al. B(1) destructive interferences and spatial phase patterns at 7 T with a head transceiver array coil. Magn Reson Med. 2005;54:1503–1518. [PubMed: 16270333]
35. Insel TR, Landis SC, Collins FS. Research priorities. The NIH BRAIN initiative. Science. 2013;340:687–688. [PubMed: 23661744]
36. Ugurbil K. Imaging at ultrahigh magnetic fields: history, challenges, and solutions. Neuroimage. 2018;168:7–32. [PubMed: 28698108]
37. De Martino F, Yacoub E, Kemper V, et al. The impact of ultra-high field MRI on cognitive and computational neuroimaging. Neuroimage. 2018;168:366–382. [PubMed: 28396293]

38. Dumoulin SO, Fracasso A, van der Zwaag W, Siero JCW, Petridou N. Ultra-high field MRI: advancing systems neuroscience towards mesoscopic human brain function. Neuroimage. 2018;168:345–357. [PubMed: 28093360]
39. Polimeni JR, Uludag K. Neuroimaging with ultra-high field MRI: present and future. Neuroimage. 2018;168:1–6. [PubMed: 29410013]
40. He X, Erturk MA, Grant A, et al. First in-vivo human imaging at 10.5T: imaging the body at 447 MHz. Magn Reson Med. 2020;84:289–303. [PubMed: 31846121]
41. Sadeghi-Tarakameh A, DelaBarre L, Lagore RL, et al. In vivo human head MRI at 10.5T: a radiofrequency safety study and preliminary imaging results. Magn Reson Med. 2020;84:484–496. [PubMed: 31751499]
42. Erturk MA, Wu X, Eryaman Y, et al. Toward imaging the body at 10.5 tesla. Magn Reson Med. 2017;77:434–443. [PubMed: 27770469]
43. Nowogrodzki A. The world's strongest MRI machines are pushing human imaging to new limits. Nature. 2018;563:24–26. [PubMed: 30382222]
44. Budinger TF, Bird MD, Frydman L, et al. Toward 20 T magnetic resonance for human brain studies: opportunities for discovery and neuroscience rationale. MAGMA. 2016;29:617–639. [PubMed: 27194154]
45. Gemert JHFV, Brink W, Webb A, Remis R. An efficient methodology for the analysis of dielectric shimming materials in magnetic resonance imaging. IEEE Trans Med Imaging. 2017;36:666–673. [PubMed: 27831868]
46. Wu X, Tian J, Schmitter S, Vaughan JT, Ugurbil K, Van de Moortele PF. Distributing coil elements in three dimensions enhances parallel transmission multiband RF performance: a simulation study in the human brain at 7 Tesla. Magn Reson Med. 2016;75:2464–2472. [PubMed: 26997332]
47. Guerin B, Adalsteinsson E, Wald LL. Local SAR reduction in multi-slice pTx via "SAR hopping" between excitations. In: Proceedings of the 20th Annual Meeting of ISMRM, Melbourne, Australia, 2012. p 642.
48. Ugurbil K. Magnetic resonance imaging at ultrahigh fields. IEEE Trans Biomed Eng. 2014;61:1364–1379. [PubMed: 24686229]
49. Shajan G, Kozlov M, Hoffmann J, Turner R, Scheffler K, Pohmann R. A 16-channel dual-row transmit array in combination with a 31-element receive array for human brain imaging at 9.4 T. Magn Reson Med. 2014;71:870–879. [PubMed: 23483645]
50. Ugurbil K, Auerbach E, Moeller S, et al. Brain imaging with improved acceleration and SNR at 7 Tesla obtained with 64-channel receive array. Magn Reson Med. 2019;82:495–509. [PubMed: 30803023]

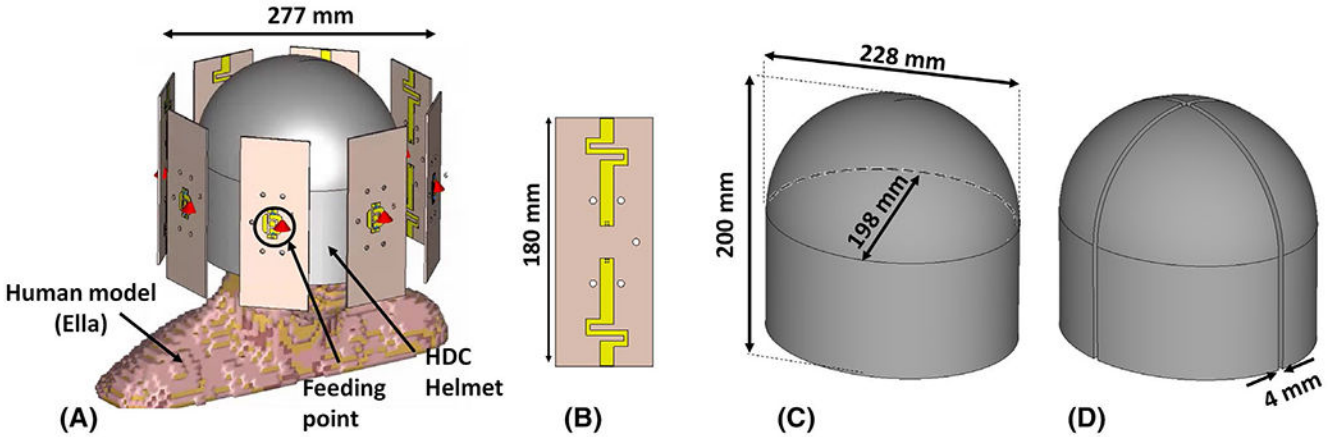

FIGURE 1.

A, The simulation setup includes a eight-channel fractionaled-dipole antenna array, a high dielectric constant (HDC) helmet and a human head model (Ella). B, Schematic of fractionated-dipole antenna. C, The HDC helmet 1 is a continuous structure with 8-mm thickness and permittivity of 78. D, Helmet 2 consists of four identical pieces of HDC material with the same geometry and permittivity of helmet 1. The 4-mm gaps between the four pieces have the permittivity of free space

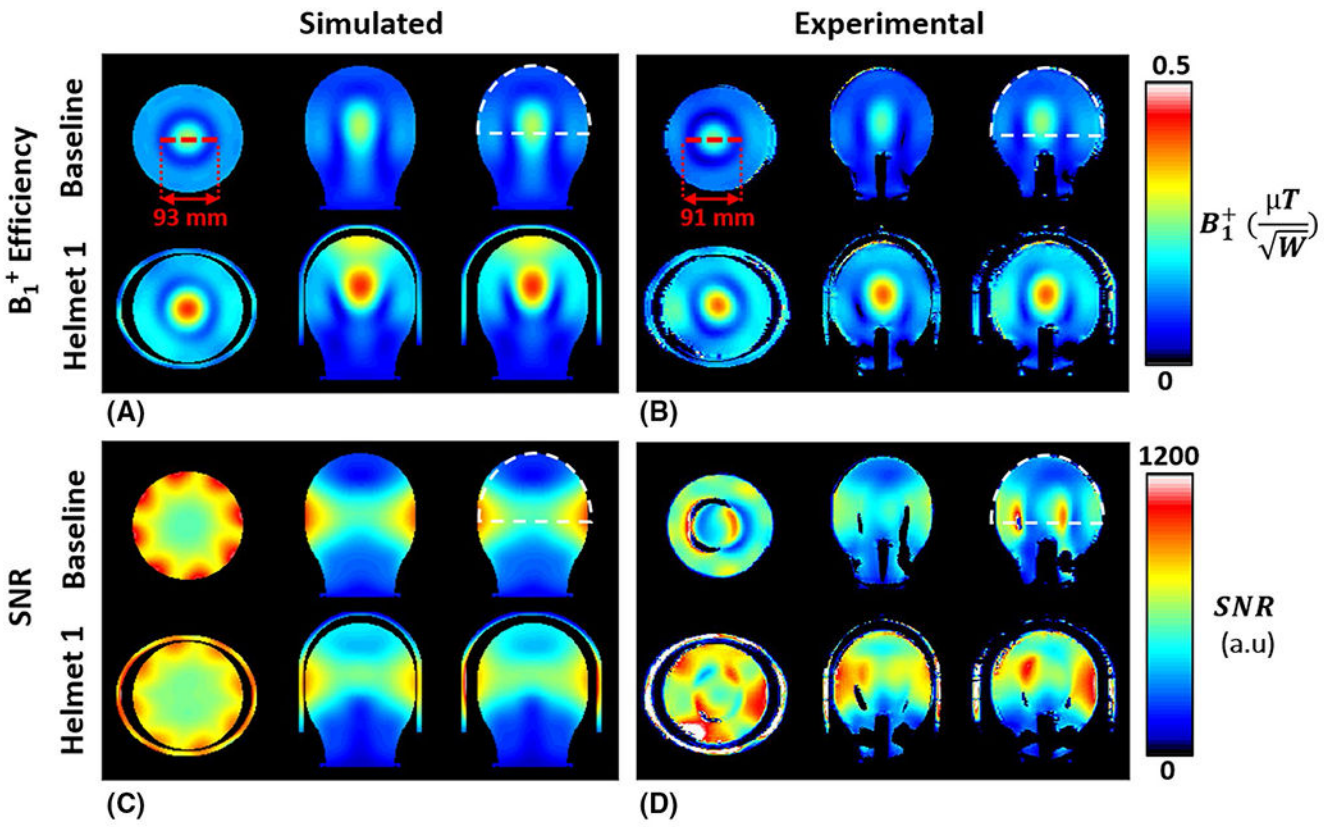

FIGURE 2.

Simulated (A,C) and experimental (B,D) transmit B_1^+ efficiency and SNR maps in a phantom without and with HDC helmet 1. The region of interest (ROI) used for quantification is the top portion of the phantom, 13 cm from apex, as indicated by the white dashed-line semicircle on the sagittal plane for baseline. This ROI approximates the space that would be occupied by the human brain with a human head in the coil. The red lines in the baseline B_1^+ efficiency maps in the axial plane indicate the outer diameter of the dark ring. Note: In the experimental maps, there is a rectangular dark region that can be seen near the bottom of phantom in the experimental coronal and sagittal maps, which is absent in the corresponding simulated maps. The rectangular dark region in the experimental maps is optical fiber leads in the phantom used for temperature mapping measurement, which was not included in our computer model

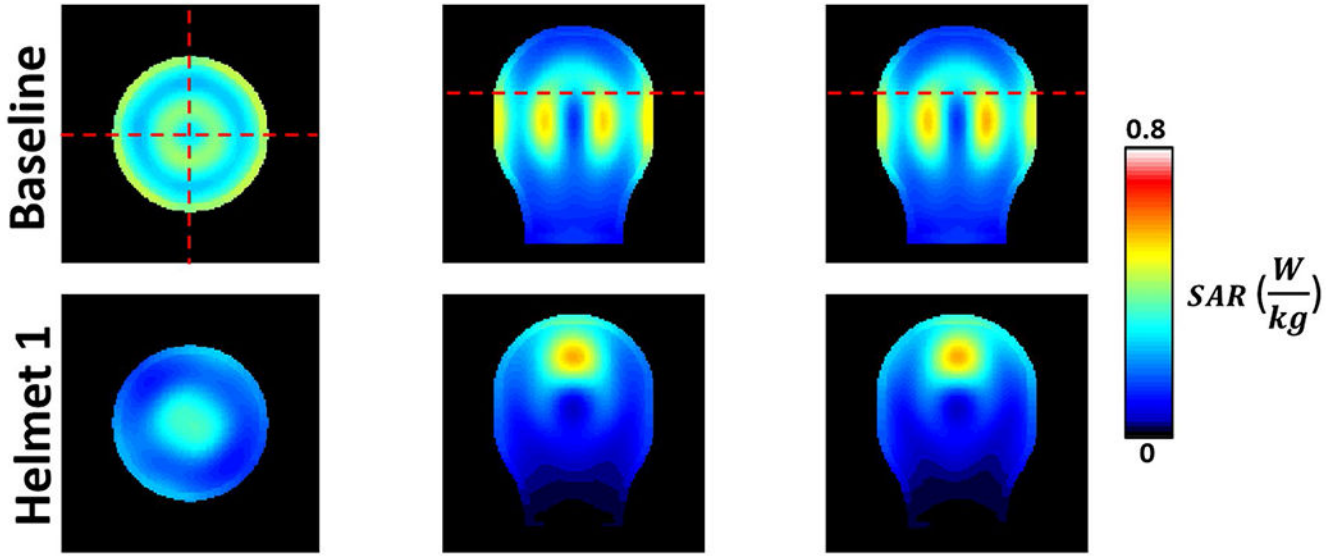

FIGURE 3.
Specific absorption rate (SAR) maps in the phantom for baseline and HDC helmet in the three orthogonal planes as in indicated (dotted lines in the upper row indicate the relative locations of the planes)

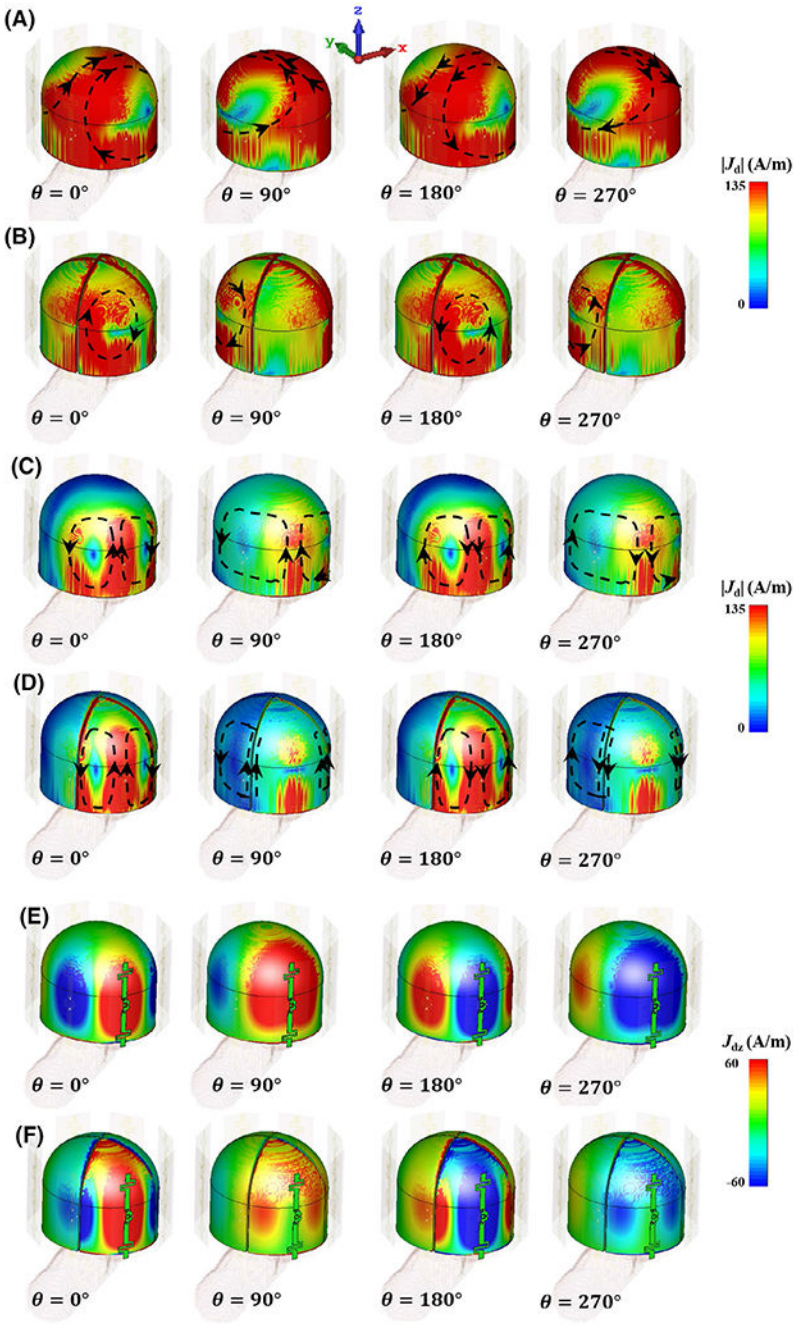

FIGURE 4.

The displacement current distributions induced by the dipole array (not shown) on the helmet 1 (A) and helmet 2 (B) at four phases (0, 90, 180 and 270). The magnitude $|J_d|$ and direction of the instantaneous displacement current at the given phases are indicated by the color scale and the vector plot (black dashed line with arrows), respectively. The persistent displacement current on the apex of helmet 1 was eliminated by dividing the continuous HDC helmet into four segments. To illustrate the propagating wave behavior explicitly, the corresponding instantaneous $|J_d|$ distributions by a single element of the dipole array are

shown in (C) and (D). In addition, the corresponding z component, J_{dz}, is also shown in (E) and (F) in each helmet. In this case, J_{dz}, the major component that produces the transverse B_1, can be seen propagating around the helmet, which is significantly attenuated by the discontinuity across the gaps in the segmented helmet. See Supporting Information Figure S1 for a more detailed temporal evolution of the displacement current in the two helmet designs

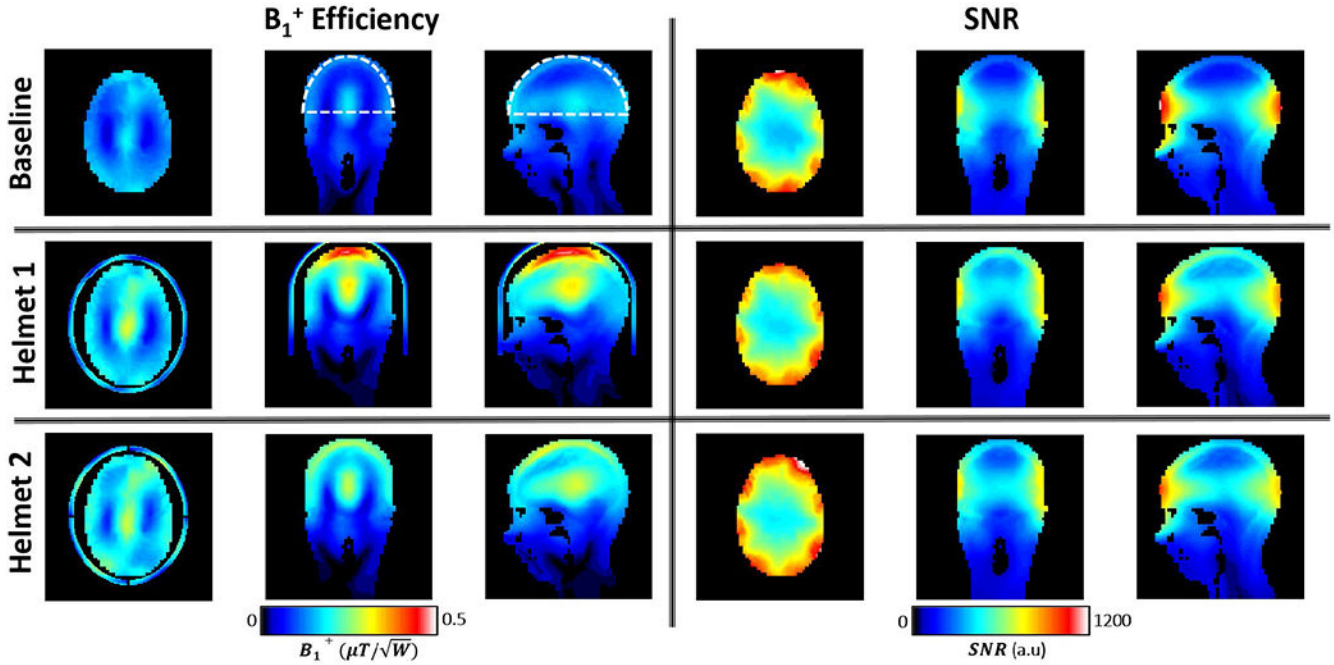

FIGURE 5.

B_1^+ efficiency and SNR maps for baseline, and with HDC helmet 1 and helmet 2. With helmet 1 (middle row), overall B_1^+ and SNR are enhanced in the head model as in the phantom. The dashed white semicircle (top row, B_1^+ efficiency map) indicates the ROI used for quantitative analysis. With HDC helmet 2 (bottom row), the intense enhancement seen with helmet 1 on the top of the brain is clearly reduced

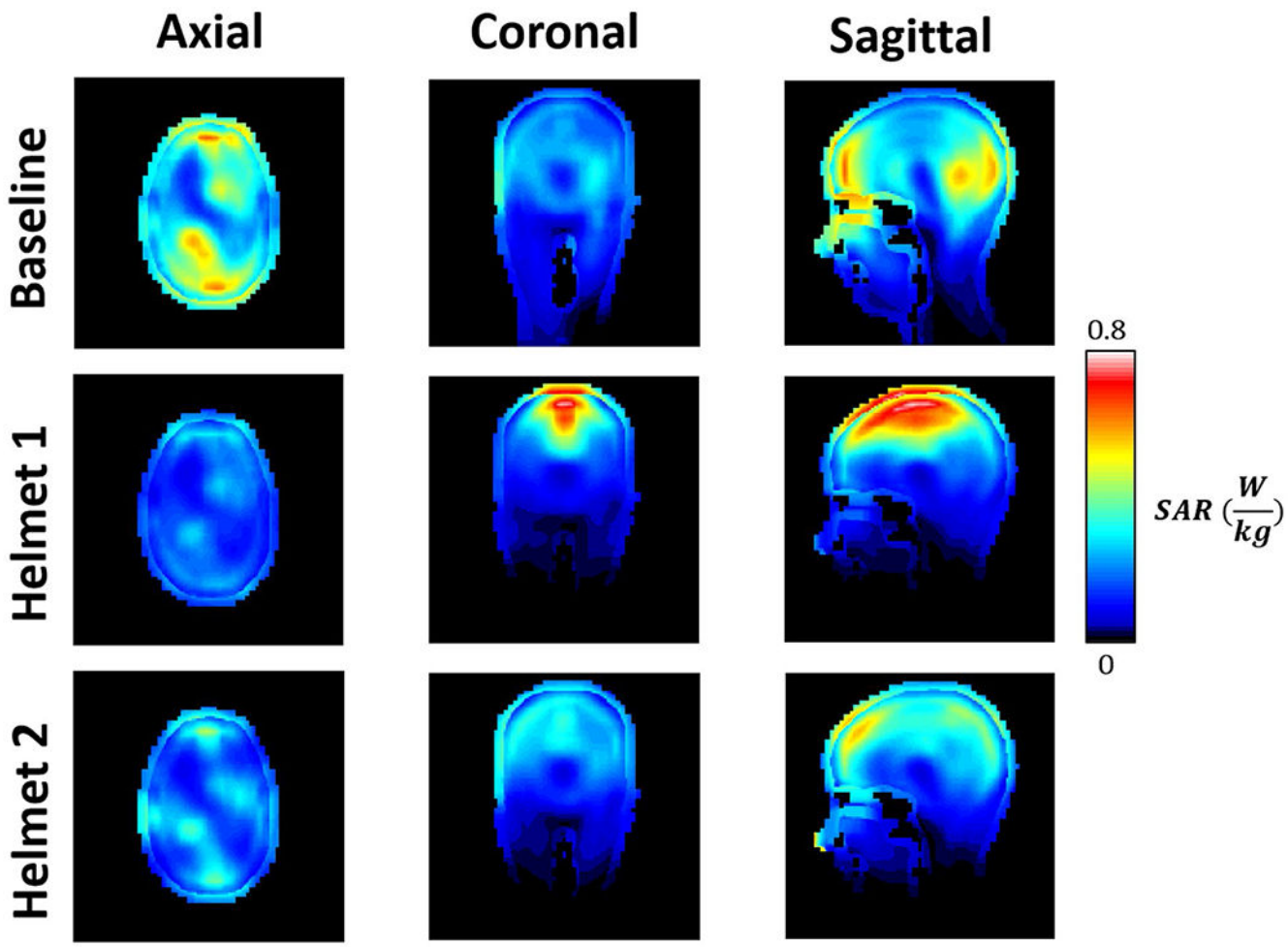

FIGURE 6.
The SAR maps in the human head model for the baseline (first row) and with HDC helmet 1 (second row) and helmet 2 (third row) at three orthogonal planes

TABLE 1

Experimental B_1^+ efficiency and SNR in the phantom for the baseline and HDC helmet 1

	Baseline	Helmet 1	Enhancement
B_1^+ efficiency ($\mu T/\sqrt{W}$)	0.11 ± 0.04	0.16 ± 0.05	47%
SNR (a.u.)	472 ± 199	684 ± 281	45%

TABLE 2

Average and SDs of simulated B_1^+ efficiency, SNR, and SAR in the human brain for baseline, HDC helmet 1, and helmet 2

	Baseline	**Helmet 1**	**Helmet 2**
B_1^+ efficiency ($\mu T/\sqrt{W}$)	0.09 ± 0.03	0.15 ± 0.08	0.14 ± 0.06
SNR (a.u.)	525 ± 120	628 ± 77	824 ± 152
Average 10g-SAR (W/kg)	0.26	0.28	0.24
Max 10g-SAR (W/kg)	0.78	0.79	0.56